Modelling the orthogonal cutting of UD-CFRP composites:

Abena, Alessandro; Soo, Sein; Essa, Khamis

DOI:
10.1016/j.compstruct.2017.02.030

Document Version
Peer reviewed version

Citation for published version (Harvard):
Abena, A, Soo, S & Essa, K 2017, 'Modelling the orthogonal cutting of UD-CFRP composites: Development of a novel cohesive zone model', *Composite Structures*, vol. 168, pp. 65-83.
https://doi.org/10.1016/j.compstruct.2017.02.030

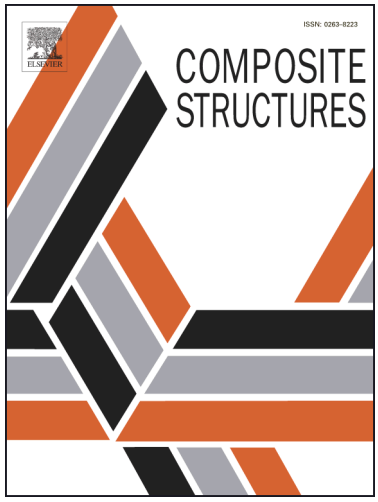

Modelling the orthogonal cutting of UD-CFRP composites: Development of a novel cohesive zone model

Alessandro Abena, Sein Leung Soo, Khamis Essa

PII: S0263-8223(16)32115-8
DOI: http://dx.doi.org/10.1016/j.compstruct.2017.02.030
Reference: COST 8251

To appear in: *Composite Structures*

Received Date: 12 October 2016
Revised Date: 21 November 2016
Accepted Date: 7 February 2017

Please cite this article as: Abena, A., Soo, S.L., Essa, K., Modelling the orthogonal cutting of UD-CFRP composites: Development of a novel cohesive zone model, *Composite Structures* (2017), doi: http://dx.doi.org/10.1016/j.compstruct.2017.02.030

Modelling the orthogonal cutting of UD-CFRP composites: Development of a novel cohesive zone model

Alessandro Abena, Sein Leung Soo, Khamis Essa*

Department of Mechanical Engineering, School of Engineering, University of Birmingham, U.K.

Abstract

The inhomogeneous and anisotropic nature of CFRP presents a challenge achieving accurate simulations largely due to limitations of current material constitutive relationship, in particular for predicting debonding of the matrix and fibre. Following a comprehensive review of the various published cohesive models a new approach for representing the fibre-matrix interface is proposed for a three-dimensional FE model of orthogonal cutting of UD-CFRP. While severe deformations of the cohesive elements are generally observed when surrounding elements fail, excessively strong bonds are typically formed when employing surface-based cohesive behaviour. The proposed approach overcomes these limitations by employing zero thickness cohesive elements based on a traction-separation law, which are deleted from the analysis if any of the surrounding elements fails. The FE models were validated in terms of predicted cutting and thrust forces against published data for different fibre orientations. Cutting forces showed good agreement to experimental results for 90°and 135°(error within 5%), while thrust forces are generally underestimated.

Keywords: Cohesive zone, Carbon Fibre Reinforced Composites (CFRP), Orthogonal cutting, Finite Element

*Corresponding author

Email address: K.E.A.Essa@bham.ac.uk (Khamis Essa)

1. Introduction

Fibre reinforced plastic (FRP) composites are increasingly replacing conventional materials in various industrial applications due to their superior properties (e.g. specific strength and specific stiffness) and flexibility for design, allowing a reduction in the number of components thereby simplifying product assembly. Although parts made from composite materials can generally be fabricated near net shape, machining operations are still required for removing excess material to meet dimensional tolerances or producing holes for joining. The machining of composite materials however usually leads to the formation of defects that can significantly compromise component integrity and performance while in service. Such defects can arise in each phase of the material, which includes matrix cracking, matrix burning, fibre fracture, fibre pullout, fibre-matrix debonding and delamination.

Different approaches encompassing experimental, empirical, analytical and numerical methods have been utilised to investigate the machining of composite materials. The numerical approach however appears to be the most promising and capable, especially in terms of capacity to analyse the process mechanics at varying levels of complexity and provides additional information that would be difficult to obtain using alternative techniques. However, the requirement for detailed material properties and very complex models leading to very high CPU time, represents a major challenge in the numerical approach. Moreover, in order to obtain reliable results, validation against experimental data is necessary.

The majority of numerical models reported in the literature describe the composite material at macroscopic [1–4] or microscopic [5, 6] length scale. The former involves representing the composite workpiece as an equivalent homogeneous material (EHM) that provides only general information on the chip formation mechanism (Figure 1(a)), whereas the microscopic or micromechanical approach accounts for each material phase separately, thus enabling more detailed simulation/analysis of material behaviour and defect formation during machining (Figure 1(b) and Figure 1(c)). The advantage of using the microscopic approach is also highlighted in work by Rentsch *et al.* [7] where a comparison with the EHM approach is realized for the orthogonal cutting of UD-CFRP and is shown in Figure 2. However, the microscopic approach entails considerable computational cost, which has led several researchers to develope a "meso-scale" formulation [8–10]. Here, the microscopic model is implemented around the vicinity of the tool with the

EHM approach for the rest of the model, in order to provide the necessary stiffness while minimising the computational cost. Hence, the micromechanical model represents a powerful approach for analysing processes at the microscopic level, but is still computationally prohibitive for simulating machining operations involving a large amount of material such as drilling, where the EHM approach has been used [11–13]. While the microscopic approach is able to simulate the behaviour of few fibres inside a ply of a composite material, the EHM approach allows implementing the stacking sequence of the plies each one with a specific orientation of the fibres. Here, the bond between the adjacent plies is realized by implementing a "cohesive zone model". It has been utilised by Santiuste *et al.* [3] to study the out-of-plane failure of composites during orthogonal cutting of LFRP composites, and also implemented to simulate delamination both for more complex machining operations such as drilling [14, 15] than for impact problems on composites [16, 17]. Recently, several studies have focused on the development of more accurate and realistic cohesive models by introducing a dependence on strain rate [18] and an elasto-plastic phase in the constitutive law [19], or implementing new approaches for the interface simulation such as the smoothed particle hydrodynamics (SPH) method [20].

The cohesive zone model has been also used in the micromechanical approach for modelling the matrix-fibre link, which is crucial for simulating debonding of the phases. It can be realized either through use of cohesive elements [6, 9, 10, 21], or by defining the cohesive property in the contact between fibre and matrix [22].

Cohesive elements based on the traction-separation law are generally used to simulate very thin adhesive layers of bonded surfaces, and implemented with a thickness value of zero [9, 10]. The limitation of this approach resides in its inability to represent damage initiation and propagation to failure under compression, and the inability to produce any stress related to a membrane response [23]. In contrast, elements representing the surrounding phases (matrix and fibre) are able to fail under compression and membrane response, and therefore deleted during the analysis. Therefore, the cohesive elements could remain in the model even if their surrounding elements fail. When this happens the cohesive elements lose their purpose, since they are not linking matrix and fibre any more, and they also usually experience excessive distortion since their nodes become free to move.

Recent researches have tried to overcome these drawbacks by extending the constitutive behaviour of the cohesive elements already implemented in

the software [21] or using traditional continuum elements for the interface [8, 24], but it is possible to assert that the behaviour previously described is generally common to all models reported in literature in which interface elements are implemented whenever surrounding elements fail earlier, independently by their ability to experience compressive deformation and failure [8, 21, 24]. In addition, the introduction of a thickness in the interface elements to simulate the compressive behaviour [8, 21, 24] did not properly represent the real interface in the composite material. In fact, generally the composite materials are realized via impregnating the fibre in the resin. Hence, the bond between the matrix and fibre is due purely to adhesion rather than a separate third phase having a finite thickness. For this reason, a cohesive model employing zero thickness cohesive elements based on the traction-separation law is a more appropriate solution.

Drawbacks shown by interface elements can be overcome implementing "surface-based cohesive behaviour", where the cohesive behaviour is defined in terms of surface interaction property avoiding implementing interface elements between fibre and matrix phases. If the absence of cohesive elements represents an advantage from a practical point of view, on the other hand it makes very difficult to recognise the interface failure, the debonding depth, and analyse the interface behaviour. In addition, this approach can be used only when a three-dimensional model is developed.

It is clear from the literature that different methods have been used in order to simulate the interface between the matrix and fibre when the micromechanical approach is chosen, each of them presenting some disadvantages. In order to overcome these limitations, the current work aims to realize a 3D model of the orthogonal cutting of unidirectional carbon fibre reinforced polymer composite by introducing, via bespoke subroutine, a novel fibre-matrix interface behaviour. Zero thickness cohesive elements based on traction-separation law are employed and deleted from the simulation if any of the surrounding elements, matrix or fibre, fails. The present work also provides, for different fibre orientations (0°, 45°, 90°and 135°), a comparison of the proposed new approach against previously published models. The comparison also attempts to provide a better understanding of each cohesive model, due to the lack of qualitative descriptions of the interface behaviour in the literature.

2. A novel approach for cohesive zone modelling

The cohesive zone model incorporating zero thickness cohesive elements based on traction-separation law is an approach that can potentially represent the actual interface behaviour due to its ability for describing very thin adhesive phases such as those present between the matrix and fibre of composite materials. In addition, it simplifies the quantitative and qualitative analysis of the interface behaviour at the post-processing stage. This method was used as the basis to develop a novel interface model that overcomes the limitations of current simulations as previously discussed. A detailed description relating to the constitutive behaviour of the proposed approach is presented in the following sections.

2.1. Elastic behaviour

For three-dimensional problem the cohesive element possesses three components of separation: one acting along the thickness direction and representing the normal behaviour of the element and two acting in the plane orthogonal to the thickness direction and representing the shear behaviour of the element. The mechanical response, for normal (tensile and compressive) and tangential (shear) behaviour, is shown in Figure 3.

Normal and shear behaviour is composed by a linear elastic response where the strains ϵ (tensile, compressive and shear) are related to displacements δ by means Equation (1):

$$\epsilon_n = \frac{\delta_n}{T_0}, \epsilon_s = \frac{\delta_s}{T_0}, \epsilon_t = \frac{\delta_t}{T_0} \tag{1}$$

where T_0 represents the constitutive thickness assumed to be unity to make the strains and displacements coincident, while the subscripts n, s and t indicate the normal and the two shear directions respectively. So, the linear elastic behaviour can be expressed by mean Equation (2):

$$\bar{t} = \begin{Bmatrix} t_n \\ t_s \\ t_t \end{Bmatrix} = \begin{bmatrix} P_n & 0 & 0 \\ 0 & P_s & 0 \\ 0 & 0 & P_t \end{bmatrix} \begin{Bmatrix} \epsilon_n \\ \epsilon_s \\ \epsilon_t \end{Bmatrix} = \overline{\overline{P}}\bar{\epsilon} \tag{2}$$

where $\bar{t}$, $\overline{\overline{P}}$ and $\bar{\epsilon}$ represent the stress vector, the stiffness matrix and the strain vector, respectively. The terms out of the diagonal have been set to zero leading to uncoupled traction-separation behaviour.

In addition to the elastic behaviour, during the analysis the cohesive element can fail, and the failure can be promoted by:

- damage initiation and evolution;
- a surrounding element failure.

2.2. Damage initiation and evolution

The end of the linear elastic behaviour is indicated by the initial damage condition (point 2), which is followed by the damage evolution. The latter represents the degradation of the adhesive phase until failure (point 4), and is obtained through the reduction of its stiffness according to Equation (3):

$$P^d_{n/s/t} = P_{n/s/t}(1 - d_{n/s/t}) \tag{3}$$

where $d_{n/s/t}$ represents the damage variable introduced for each failure mode. It is expressed by the Camanho and Davila law [25] describing a linear damage evolution:

$$d_{n/s/t} = \frac{\delta^f d_{n/s/t}(\delta^{max}_{n/s/t} - \delta^0_{n/s/t})}{\delta^{max}_{n/s/t}(\delta^f_{n/s/t} - \delta^0_{n/s/t})}, \qquad d_{n/s/t} \in [0,1] \tag{4}$$

where $\delta^0_{n/s/t}$, $\delta^f_{n/s/t}$ and $\delta^{max}_{n/s/t}$ represent the displacement at the damage initiation, the displacement at failure and the maximum displacement reached during the analysis until the time considered, respectively. The segment $\overline{03}$ reported in Figure 3 represents the unloading condition once initiation of damage. In the present work, the damage initiation condition has been chosen to be based on the quadratic nominal stress criterion, coupling traction and shear behaviour as in Equation (5):

$$\left\{\frac{\langle t_n \rangle}{t^0_n}\right\}^2 + \left\{\frac{\langle t_s \rangle}{t^0_s}\right\}^2 + \left\{\frac{\langle t_t \rangle}{t^0_t}\right\}^2 = 1 \tag{5}$$

where the Macaulay brackets $\langle\rangle$ mean that no damage initiation is possible under compressive behaviour. With this assumption, the softening behaviour in the cohesive element may be start before each mode reaches its damage initiation condition.

Traction and shear behaviour interaction has been considered also in terms of failure condition, implementing the power law criterion:

$$\left\{\frac{G_n}{G_n^C}\right\}^{\alpha} + \left\{\frac{G_s}{G_s^C}\right\}^{\alpha} + \left\{\frac{G_t}{G_t^C}\right\}^{\alpha} = 1 \tag{6}$$

where G^C represents the fracture energy, i.e. the area below the stress-displacement curve in Figure 3. When Equation (6) is satisfied, the integration point of the cohesive element is considered failed. The cohesive element is deleted from the analysis when all the integration points fail.

2.3. Failure due to connectivity

Cohesive element failure during the analysis could be also due to surrounding element failure. As the analysis starts, the connectivity matrices $\overline{\overline{CM}}$ and $\overline{\overline{CF}}$, storing the connection between cohesive elements and surrounding elements (matrix and fibre respectively), are created by mean of a user defined field subroutine (VUSDFLD). For that goal, the VUSDFLD subroutine calls the appositely created connectivity subroutine for the matrices generation, starting from the input file created by the Abaqus/CAE. In fact, the subroutine reads the input file looking for the sections where nodes and elements information for cohesive, fibre and matrix phases are stored. After, it creates two different matrices for each phase: elements matrix $\overline{\overline{El}}_{phase-name}$, and the nodes matrix $\overline{\overline{Nd}}_{phase-name}$. The elements matrix $\overline{\overline{El}}_{phase-name}$ stores for each element of the considered phase the ID element number and the ID numbers of the eight nodes forming the 3D element. The matrix is composed by nine rows and columns number equal to the total elements number in the considered phase. For each column, the first row represents the element ID number, while the following eight the ID numbers of all nodes forming the element. Instead, the $\overline{\overline{Nd}}_{phase-name}$ matrix stores for each node of the considered phase the ID node number and its three spatial coordinates. The matrix is composed by four rows and columns number equal to the total nodes number in the considered phase. For each column, the first row contains the node ID number, while the following three the spatial coordinates of the node. It is possible to observe that the $\overline{\overline{El}}_{phase-name}$ and $\overline{\overline{Nd}}_{phase-name}$ matrices dimension changes depending by the phase considered. In the end, six matrices are built: $\overline{\overline{El}}_{cohesive}$, $\overline{\overline{El}}_{fibre}$, $\overline{\overline{El}}_{matrix}$, $\overline{\overline{Nd}}_{cohesive}$, $\overline{\overline{Nd}}_{fibre}$, and

$\overline{\overline{Nd}}_{matrix}$. Starting from these matrices, the connectivity subroutine compares each cohesive element with all fibre and matrix elements at the nodes coordinates level. Finally, the subroutine is able to create two different connectivity matrices for fibre and matrix phases having number of row equal to the cohesive elements number in the model and two columns. The first column contains the cohesive elements ID number, while the second reports the correspondent connected surrounding elements that satisfy the condition previously mentioned. The Connectivity matrices are after available in the VUSDFLD subroutine.

During the analysis the cohesive elements follow the elastic behaviour and damage evolution. In the meanwhile, matrix and fibre deform under the loads applied during the machining, and eventually fail. As one matrix/fibre element fails, the VUSDFLD subroutine searches in the connectivity matrices for the possible corresponding cohesive element, deleting it from the analysis.

This criterion allows avoiding the cohesive element can remain in the model after the surrounding element fails, losing its purpose and potentially experiencing excessive deformation.

3. Finite element model

A 3D finite element analysis of orthogonal cutting on UD-CFRP was developed using Abaqus/Explicit software and referring to Calzada *et al.* [8] work. The three-dimensional model was obtained by mean extrusion of the two-dimensional model presented in Abena *et al.* [21] work where meso-scale approach was implemented. A schematic of the FEM model and the boundary conditions applied are reported in Figure 4. The materials behaviour was implemented as reported in Abena *et al.* [21]. In fact, the epoxy matrix was implemented according to a static compressive stress-strain curve at room temperature and the element in the model was considered failed when the Von Mises stress reaches the ultimate stress level, while the carbon fibres were simulated as transversely isotropic and perfectly elastic to failure with failure criterion based on the maximum principal stress. The material properties are reported in Table 1.

Contact conditions were implemented through general contact algorithm, where the penalty method was used to enforce the contact constraint between surfaces. The contact property was defined in terms of Coulomb model considering a constant friction coefficient equal to 0.3 for all fibre orientations. Tie constraint was implemented between the EHM and micromech-

Table 1: Material properties [8, 9, 25, 26]

Material	Property	Value
Carbon fibre	Elastic constants	E_1=235 GPa, E_2=E_3=14 GPa
		$\nu_{12} = \nu_{13}$=0.2, ν_{23}=0.25
		G_{12}=G_{13}=28 GPa, G_{23}=5.5 GPa
	Longitudinal strength	X_t=3.59 GPa, X_c=3 GPa
Epoxy	Elastic constants	E=2.96 GPa, ν=0.4
	Yield strength	σ_y=74.7 MPa
Interface	Normal strength	σ_{max}=167.5 MPa
	Shear strength	τ_{max}=25 MPa
	Fracture energy	G^c=0.05 N/mm^2
EHM	Elastic constants	E_1=142.184 GPa, E_2=E_3=7.606 GPa
		$\nu_{12} = \nu_{13}$=0.28, ν_{23} ==0.347
		G_{12}=G_{13}=4.151 GPa, G_{23}=2.824 GPa

anical zone, and also between adjacent phases (matrix, fibre and cohesive) except when employing the surface-based cohesive behaviour. The mesh in the micromechanical area was realized by employing 3D Stress Hex elements and setting the mesh seed on the edges equal to 1 μm. In order to reduce the computational cost of the analysis coarse mesh was used in the EHM zone. In addition, the Mass Scaling technique was employed to speed up the analysis. Finally, the machining parameters implemented in the simulation are reported in Table 2.

Table 2: Machining Parameters

Tool	5 μm edge radius
	10°clearance angle
	25°rake angle
Cutting speed	500 mm/min
Depth of cut	15 μm
Fibre orientations	0°, 45°, 90°, 135°
Fibre diameter	7.5 μm
Fibre volume percentage	60 %

The new proposed model for the interface simulation (Novel Approach)

has been compared with previously published models:

- Approach 1: zero thickness cohesive elements based on traction-separation law [10];
- Approach 2: cohesive elements based on traction-separation law presenting a small thickness [21];
- Approach 3: surface-based cohesive behaviour [22];

Abena *et al.* [21] developed the Approach 2 to overcome the limitations represented by the excessive deformation of the cohesive elements in the Approach 1, usually implemented in literature, due to earlier failure of surrounding elements (matrix, fibre). A small thickness (0.25 μm) was introduced in order to accommodate the deformation under compression until failure. Differently by Abena *et al.* [21], a linear behaviour under compression is considered. The failure condition is implemented through a user defined field subroutine (VUSDFLD), allowing the deletion of the cohesive element when the compressive failure stress is reached in each integration point. It is important to notice that the element thickness value is strictly dependent by the compression displacement at failure.

Instead, Chennakesavelu *et al.* [22] implements the surface-based cohesive behaviour where no elements are present for the interface. Using this approach Chennakesavelu *et al.* avoid interface elements could eventually remain in the model losing their purpose and potentially experiencing excessive distortion.

4. Results and discussion

Several analyses were carried out for different fibre orientations and interface approaches. A comparison in terms of cohesive behaviour has been performed, and models are validated in terms of cutting and thrusst forces against published experimental results [8]. In the end, also the computational time has been analysed in order to possibly identify a preferred cohesive model.

4.1. Cohesive behaviour

Approach 1: Zero thickness cohesive elements based on traction-separation law. The zero thickness cohesive elements based on the traction-separation

law (Approach 1) are implemented for 90°fibre orientation. The results highlight how the cohesive elements allow to simulate the debonding defect being able to work under tensile and shear behaviour, but their inability to fail under compression and the assumption the membrane response does not produce any stress lead to an undesired behaviour highlighted in Figure 5. In fact, Figure 5(a) shows how matrix and fibre elements ahead of the tool fail mainly because of compressive stress due to the tool progression, while the cohesive elements remain in the model. After that, the tool continues to move forward stretching the cohesive elements which experience excessive deformations, as it is shown in Figure 5(b).

The cohesive elements failure is also due to the tool action that, pushing fibres and matrix ahead of it, causes the interface elements stretching in the already machined area below the cutting plane originating debonding defects (Figure 6). Analysing the failure mechanism of cohesive elements that undergo tensile behaviour the shear stress represents the main contribution to the damage initiation in the elements. This is due to the low shear stress limit required to reach the shear damage initiation when compared with the normal behaviour. So, small shear deformations can immediately give a big contribution in reaching the damage initiation respect to the normal displacements. Even during the damage evolution the shear stress contributes mainly to the elements failure, since the normal stress remains low. However, cohesive failure extends for few fibres ahead of the tool also below the cutting plane near the areas where matrix and fibre damage takes place due to excessive deformation caused by surrounding elements deletion.

Approach 2: Cohesive elements based on traction-separation law having a small thickness. In order to overcome the drawback of the previous approach, a small thickness was introduced in the cohesive elements in order to accommodate compressive deformation and failure leading to the Approach 2, showed in Figure 7.

Differently from what it is shown in Figure 5(a), the capacity of the cohesive elements to behave and fail under compression can be observed in Figure 8, where the red lines mark the depth of the debonding defects for the time-step considered. It is important to notice that the introduction of this new failure condition changes the model behaviour during the simulation. In fact, the compressive failure of cohesive elements is not localized, but it extends for many fibres ahead of the tool. So, while in the previous approach the link between fibre and matrix is still active ahead of the tool after few

fibres, in this case fibres and matrix above the red marks are totally separated and able to move independently also very far from the tool (Figure 8). The cohesive damage extends not only in the cutting direction, but also below the cutting plane ahead of the tool originating debonding defects due to compression failure. It is important to underline that during compression the element can still experience shear deformation that can lead to failure. In this case compressive and shear behaviour are uncoupled in terms of damage initiation and evolution. However, the compressive stress is so high that the compressive failure is generally reached before the shear failure. Further debonding is than formed below the cutting plane after the tool is passed like the previous approach. In this case, the shear behaviour is still representing the main contribute to the damage initiation mechanism, after which the tensile normal stress increases contributing together to shear to reach the failure condition.

The fibre experiences a multi-fracture damage which occurs at two different locations. The tool movement causes the first crack formation at the contact point with the fibre since the fibre is compressed between the tool and the following matrix. This crack is not extended for all fibre thickness because, at some point, the matrix behind starts to fail under compression allowing the fibre to increase the bending deformation under the tool movement. Due to bending stresses, a second crack rises and propagates along the whole fibre thickness below the cutting plane. After that, the matrix continues to fail until the two consecutive fibres become in contact. When this happens, the first crack in the first fibre continues to propagate through the fibre for all thickness length. So, the first fibre is divided in three parts. Further, tool movement causes the fragmentation of the upper part of the first fibre and the bending of the following fibre. After that the chip formation mechanism repeats cyclically. So, during the cutting, subsurface damages in terms of fibre and matrix failure are also formed in the machined workpiece as visible in Figure 8.

Differently from 90°, when 45°fibre orientation is considered the chip formation mechanism totally changes, as it is shown in Figure 9. The tool force could be decomposed in two components: one in the fibre direction and the other orthogonally to it. The latter component compresses the different phases leading to a crack formation and propagation along the same direction in the fibre in contact with the tool, Figure 9(b). Also the cohesive elements fail under compression causing debonding formation below the cutting plane in the area highlighted by mean red markers in Figure 9(b).

This force component, compressing the phases along its direction, causes a bending deformation during failure in the phases nearer to the tool. So, the cohesive behaviour changes from compression to tension increasing the distance from the area marked with red lines. Instead, the component acting along the fibre direction introduces shear behaviour, as can be observed in Figure 9(a), leading to the interlaminar shear fracture in the elements where tensile stresses are also present. Regarding the matrix, it fails under compression starting from the point of the crack location on the previous fibre. So, matrix and fibre are divided by the tool into two different parts below the cutting plane. In addition, like for 90°the machined workpiece shows subsurface damages.

For 135°fibre orientation, the chip formation mechanism changes again. The fibre engaged by the tool undergoes bending deformation being peeled from the workpiece and causing huge deformations until failure in the cohesive elements that try to keep the fibre and previous matrix together.

The debonding defect increases with the increment of the fibre deflection, as it is shown in Figure 10, until the fibre failure takes place due to bending stress. When this happens, the tool exercises a pressure only on the upper part of the fibre, which causes the failure under compression of the following matrix. Since the following matrix is still linked by mean cohesive elements with the lower part of the broken fibre, during its failure under compression, it continues to drug with itself the lower part of the fibre increasing the bending deformation and so the debonding defect. At some point, the two consecutive fibres come in contact, and the behaviour described starts again since the tool pressure is transmitted by mean the first fibre to the second. During the tool displacement the depth of the fibre failure decreases moving towards the workpiece surface along a direction oriented orthogonally to the fibre direction. Moreover, during the cutting the fibres experience multi-fracture damage.

The cohesive elements show two different kind of failure. In the upper part of the workpiece, the tool action causes compression of different phases leading to a compressive failure of cohesive elements. Instead, below the cutting plane the cohesive elements undergo shear and tensile behaviour, with damage initiation and failure caused mainly by shear stress.

Even if the cohesive failure is crucial to estimate the debonding defect in the machined material, the damage level in the cohesive elements, which remain in the model after the machining, represents also an important parameter that needs to be investigated. In fact, during in-service condition,

the stress in the material could promote additional debonding compromising the component integrity and performance. For this goal, the SDEG variable representing the overall value of the scalar damage, and the QUADSCRT variable indicating the damage initiation condition can be used. In Figure 11 it is possible to observe how the damage in the cohesive elements extends below the debonding reaching areas that are very far from the tool. The amount of damage decrease moving away far from the cutting plane and it is possible to observe a considerably expanded zone interested by a medium/high damage value prone to fail if subjected to further stresses.

The approach previously described still presents some cohesive elements failing due to excessive distortion caused by surrounding element failure, as it is shown in Figure 10(a), where a highly deformed cohesive element is highlighted in red.

Approach 3: Surface-based cohesive behaviour. As described, the problem of the excessive distortion of the cohesive elements has been limited implementing the failure condition under compression. It needs of the introduction of a thickness in the cohesive elements. As discussed above, the introduction of a thickness in the cohesive elements and the capacity to fail under compression could not represent properly the real interface behaviour.

Alternatively to the previous approaches it is possible to implement the cohesive behaviour as a contact property (Approach 3). This approach allows eliminating the problem related to excessive deformation of cohesive elements without implementing compressive failure and thickness. If the absence of cohesive elements represents an advantage from a practical point of view, on the other hand it makes very difficult to recognise the interface failure and analyse the interface behaviour. In order to understand the interface behaviour during the cutting, two variables can be used: CSDMG variable which represents the overall value of the damage, and CSQUADSCRT variable which indicates if the damage initiation condition chosen has been satisfied.

For 90°fibre orientation, the chip formation mechanism is similar to the previously described from the failure mechanism point of view, but the velocity at what the damage propagates ahead of the tool along the cutting plane is much higher. In fact, in Figure 12(b) it is possible to notice that more fibres and matrix phases are interested by the damage at the end of the analysis when compared with Figure 11(c). Analysing the cohesive behaviour at the fibre-matrix interface, also in this case the damage propagates deeply inside

the material affecting areas very far from the tool, Figure 12(b). Debonding defect in the model is represented by nodes where the damage variable CSDMG reaches the unitary value. During the analysis this value is reached only in few nodes indicating that the fibre-matrix link is still active for most of the interfaces in the model as it is shown in 13, where areas with CSDMG variable values between 0.99 and 1 have been highlighted. It represents a big difference with the previous approaches where cohesive elements failure was observable during the cutting at the end of the analysis. So, using the surface based cohesive behaviour, the link between fibre and matrix appears stronger compared with cohesive elements even if the same properties are implemented. Finally, it is possible to affirm that overall no debonding is detected using the present approach.

For 45°fibre orientation, the chip formation mechanism is similar to what observed in the previous approach. Even in this case the CSDMG variable can reach high values but less than the unitary leading to an absence of debonding during the cutting.

For 135°fibre orientation, the chip formation mechanism remains similar to the previous approach. It is possible to notice that the fibre fractures in direction orthogonal to the fibre orientation, Figure 12(c), take place earlier than the previous approach and at the same time-step for all fibres, instead to have progressive failure propagation through the fibres moving towards the sample surface with the time. Differently from 45°and 90°fibre orientations, debonding formation is observed in the model on the right side of the second fibre in the red area reported in Figure 14 which extension is about 15 μm.

Also for 45°and 135°, interface damage extends below the cutting plane far from the tool.

For the surface based cohesive method also the 0°fibre orientation has been investigated, Figure 15. During the cutting the first matrix and fibre are compressed by the tool which tends also to lift up and bend them because of the rake angle. Conversely, the cohesive behaviour at the interface tends to keep the different phases together. The cohesive effect seems to predominate causing failure under compression of the first brittle fibre and bending of the first ductile matrix. The second matrix fails under compression while the second fibre is weakly pushed down by the tool.

Figure 16 shows the damage at the interfaces in the model. Damage extends ahead of the tool far from it, and differently from the other fibre orientations it remains mainly contained above the cutting plane slightly affecting the next interface. So, in this case debonding in the machined

work-piece is totally absent.

Novel cohesive model. Even if implementing the surface based cohesive method it is possible to avoid all drawbacks described before, difficulty in the interface behaviour analysis and debonding evaluation has been experienced. Also, differently from the method in which cohesive elements using traction-separation law have been implemented, a general absence of debonding has been detected. So, a new method for the interface simulation has been developed in order to obtain a robust interface model that can overcome all difficulties listed until now.

For 90°fibre orientation, failure modes experienced by fibres and matrix are similar to what described in the Approach 2. So, the fibres show multi fracture failure mode due to bending stresses and to the action of the tool that pushes the fibre against each other, while the matrix failure is due to compressive stresses exercised by the surrounding fibres. Since the classical zero thickness cohesive element approach based on traction-separation law has been implemented, the cohesive elements cannot undergo compression. In this case, it does not represent a limit in the cohesive elements behaviour. It is because, even if the surrounding matrix and fibre elements fail due to compression, the cohesive element connected with them is recognized by mean user defined field subroutine and eliminated from the analysis. So, results show no excessive deformations are experienced by cohesive elements. Figure 17 shows the area where cohesive elements have been deleted by the subroutine due to matrix failure under compression and the cohesive elements still active in the model near that area. The failure of cohesive elements is similar to what described in the Approach 1 where generally the shear stress represents the main contribution to the damage initiation. Also during the damage evolution phase the shear stress contributes mainly to the elements failure, since the normal stress remains low.

For 45°fibre orientation, even if fibres and matrix failure mechanism is quite similar to what described in the Approach 2, in this case the cohesive elements in the area undergoes compression remain active until a surrounding element fails. Due to this behaviour the different phases are kept together by the interface longer. The cohesive element failure in the model is mainly due to shear stresses originated during the cutting.

For 135°fibre orientation, like for the others fibre orientations, the failure modes in the fibres and the matrix are similar to what observed in the Approach 2, where matrix failure is mainly due to compression and fibre

failure to bending. Instead, the cohesive elements undergo shear and tensile behaviour, with damage initiation and failure caused mainly by shear stress.

The Figure 18 shows the amount of damage in the cohesive elements at the end of the analysis for 45°, 90°and 135°. The area affected by damage extends very far from the tool making the interface more prone to fail if subjected to further loads during the in service conditions.

In order to compare the Novel Approach and the Approach 3, also the 0°fibre orientation has been investigated. The chip formation mechanism for the Novel Approach proposed is quite different from the previous, as it is shown Figure 19. Even in this approach the tool tends to lift up the fibre and the matrix in contact with the tool rake face and to push down the phases located below the cutting plane. The difference with the previous approach is due to the cohesive elements behaviour. In fact, they tend to oppose to bending deformation trying to keep all phases together until they reach the failure condition. The tool progression causes an increment in the bending deformation and the propagation of cohesive failure along the catting direction. In the cohesive elements shear and tensile stresses contribute together to damage initiation and evolutions until failure with a bigger contribute of the shear for the damage initiation.

Differently by the other orientations, no damage has been detected below the cutting plane in the machined material.

Results obtained for 0°and 135°fibre orientations with the Novel Approach and the Approach 3 can be compared with high-speed camera images obtained by Calzada *et al.* [8] and shown in Figure 20. The failure mechanism observed experimentally shows a bending failure of the fibre for 0°fibre orientation with chip formed by fibre length between 100-150 μm. It agrees well with the behaviour of the model obtained implementing the Novel Approach even if fibre failure is not reached during the analysis, while the Approach 3 shows a compressive fibre failure due to a strong bond between different phases.

For 135°fibre orientation, the Approach 3 shows a better behaviour in terms of depth at what the fibre failure occurs, while the Novel Approach shows a better behaviour from the cohesive point of view. In fact, in the latter approach, the cohesive elements failure propagates very far from the tool as expected by the experimental results, but the fibre failure location seems to be too near to the cutting plane.

For the Novel Approach proposed it is worth to calculate the amount of debonding for each fibre orientation. For 0°fibre orientation, debonding is

experienced among different phases ahead of the tool, but no debonding is visible below the cutting plane, as Figure 19(b) shows.

For 45°, 90°and 135°fibre orientations the maximum debonding detected during the analysis are about 36 μm, 33 μm and 59 μm respectively leading to subsurface damages in the machined workpiece as it is shown in Figure 21-23.

4.2. Cutting forces validation

The numerical cutting and thrust forces for the Novel Approach and the Approach 3 are reported and compared with the experiments carried out by Calzada *et al.* [8] in Figure 24 and Figure 25, respectively. The experimental data present a force increment for fibre orientation between 0°to 45°, and a reduction after 45°until 135°.

In both approaches the numerical cutting and thrust forces are calculated as the average value over the entire analysis for each fibre orientation as shown in Figure 26 and Figure 27. In term of cutting forces the Novel approach shows a better agreement with the experimental data for all fibre orientations except for zero degrees, where it is a bit lower than the one calculated using the Approach 3. Prediction of cutting forces for 90°and 135°implementing the Novel Approach is very good. Even if both models underestimate the cutting forces for 0°and 45°, the new proposed model is able to show a more similar trend to the experimental one. Differently, the thrust forces are widely underestimated for all fibre orientations independently by the approach, even if the Novel Approach seems to provide slightly better results except for 135°. The difficulty in the thrust force prediction can be observed over the literature. This challenge can be explained considering the material behaviour during the cutting. In fact, it is divided in two regions by the tool: pressing and chipping. The material in the former region is pushed under the tool, and when the tool is passed it springs back due to the elastic recovery exerting a pressure on the clearance face and so contributing to the thrust force [27]. The difficulty in replicating this behaviour in the FEM model can explain the big gap usually observed between the experimental and numerical thrust force.

4.3. Analysis time and computational cost

The analysis time represents also an important factor that could contribute in the choice of the assumptions and approaches in the simulation. For this reason the computational time, using an Intel(R) core(TM) i7-3770 CPU

with 3.4 GHz and 32 GB of RAM, is calculated and compared for Novel Approach and the Approach 3 and reported in Figure 28. Job settings in Abaqus software have been left as default option. The computational time follows a similar trend for both approaches and it is dependent by the fibre orientation showing a considerable increment when 135°fibre orientation are simulated. Figure 28 also highlights how the Novel Approach proposed reduces the analysis time of about 12, 1.5 and 20 hours for 0°, 90°and 135°respectively. Only for 45°fibre orientation an increment of about 15 hours is detected. Moreover, the analysis time is very high in general independently by the approach despite mass scaling has been used.

5. Conclusions

A 3D model of the orthogonal cutting on CFRP composite material has been developed by mean a meso-scale model introducing a new approach for the interface simulation. The interface behaviour proposed has been compared against three different approaches used in the literature for different fibre orientations:

- zero thickness cohesive elements based on traction-separation law [10];
- cohesive elements based on traction-separation law presenting a small thickness [21];
- surface-based cohesive behaviour [22].

Implementing the Approach 1 the inability of the cohesive elements to fail under compression and the assumption that the membrane response does not produce any stress could lead to excessive element deformation during the analysis when surrounding elements fail.

In order to include compressive behaviour until failure in the cohesive elements, a small thickness has been introduced. The Approach 2 is capable to limit the excessive deformation that cohesive elements can experience making them to fail generally before their surrounding elements. When this does not happen the cohesive elements remain in the model showing big deformation. In addition, the introduction of a thickness could not reflect the physical reality and it could also change the chip formation mechanism.

The surface-based cohesive behaviour allows to overcome the drawbacks shown by previous approaches. Despite that, it makes the interface behaviour

analysis very hard. Also, debonding defect formation is almost absent or very low for all fibre orientations making the matrix-fibre link stronger when compared with cohesive elements based on traction-separetion law and high speed camera images [8].

So far, the approach that could potentially represent the real interface behaviour is the Approach 1. For this reason the authors attempted to improve it proposing a novel fibre-matrix interface behaviour. It is capable to totally avoid excessive distortion of cohesive elements connecting their failure with surrounding elements failure.

The new approach shows that for 0°fibre orientation in the cohesive elements shear and tensile stresses contribute together to damage initiation and evolutions until failure with a bigger contribute of the shear for the damage initiation. Instead for 45°, 90°and 135°fibre orientation the damage initiation and failure are generally mainly caused by the shear stress.

Cutting forces have also been calculated for the new approach and the approach implementing the surface-based cohesive behaviour for comparison purpose. Globally the new approach proposed agrees better with the experimental published data [8].

In addition, the novel approach shows also a lower CPU time for all simulations except for 45°.

Finally, the new approach proposed can be implemented also in a 2D analysis differently from the surface-based cohesive behaviour that require a 3D model to be used.

The simulations have been carried out for 30 μm cutting length. A higher value should be considered in order to highlight debonding formation inside the workpiece far from the free edges, especially for 45°fibre orientation, obtaining a more realistic debonding value. Moreover, a longer analysis is required for 0°fibre orientation in order to detect the fibre failure. Future work will also involve experimental trials in order to validate the model in terms of debonding.

References

[1] G. V. G. Rao, P. Mahajan, N. Bhatnagar, Three-dimensional macro-mechanical finite element model for machining of unidirectional-fiber reinforced polymer composites, Mat Sci Eng A 498 (2008) 142–149.

[2] J. L. Cantero, C. Santiuste, N. Marín, X. Soldani, H. Miguélez, 2D and

3D approaches to simulation of metal and composite cutting, in: AIP Conference Proceedings, vol. 1431, AIP Publishing, 651–659, 2012.

[3] C. Santiuste, A. Olmedo, X. Soldani, H. Miguélez, Delamination prediction in orthogonal machining of carbon long fiber-reinforced polymer composites, J. Reinf. Plast. Compos. 31 (2012) 875–885.

[4] C. Santiuste, X. Soldani, C. Santiuste, M. Miguélez, Machining FEM model of long fiber composites for aeronautical components, Compos. Struct. 92 (2010) 691–698.

[5] D. Nayak, I. Singh, N. Bhatnagar, P. Mahajan, An analysis of machining induced damages in FRP composites - A micromechanics finite element approach, in: AIP Conference Proceedings, vol. 712, AIP Publishing, 327–331, 2004.

[6] C. R. Dandekar, Y. C. Shin, Multiphase finite element modeling of machining unidirectional composites: prediction of debonding and fiber damage, J Manuf Sci E 130 (2008) 1–12.

[7] R. Rentsch, O. Pecat, E. Brinksmeier, Macro and micro process modeling of the cutting of carbon fiber reinforced plastics using FEM, Procedia Eng. 10 (2011) 1823–1828.

[8] K. A. Calzada, S. G. Kapoor, R. E. D. Vor, J. Samuel, A. K. Srivastava, Modeling and interpretation of fiber orientation-based failure mechanisms in machining of carbon fiber-reinforced composites, J Manuf Proces 14 (2012) 141–149.

[9] G. V. G. Rao, P. Mahajan, N. Bhatnagar, Micro-mechanical modeling of machining of FRP composites - Cutting force analysis, Compos Sci Technol 67 (2007) 579–593.

[10] G. V. G. Rao, P. Mahajan, N. Bhatnagar, Machining of UD-GFRP composites chip formation mechanism, Compos Sci Technol 67 (2007) 2271–2281.

[11] V. Palani, Finite element simulation of 3D drilling in unidirectional CFRP composite, Master's thesis, Wichita State University, 2006.

[12] O. Isbilir, E. Ghassemieh, Numerical investigation of the effects of drill geometry on drilling induced delamination of carbon fiber reinforced composites, Compos. Struct. 105 (2013) 126–133.

[13] V. Phadnis, A. Roy, V. Silberschmidt, A finite element model of ultrasonically assisted drilling in carbon/epoxy composites, Procedia CIRP 8 (2013) 141–146.

[14] V. Phadnis, F. Makhdum, A. Roy, V. Silberschmidt, Drilling in carbon/epoxy composites: Experimental investigations and finite element implementation, Composites Part A 47 (2013) 41–51.

[15] N. Feito, J. López-Puente, C. Santiuste, M. Miguélez, Numerical prediction of delamination in CFRP drilling, Compos. Struct. 108 (2014) 677–683.

[16] J. Zhang, X. Zhang, Simulating low-velocity impact induced delamination in composites by a quasi-static load model with surface-based cohesive contact, Compos. Struct. 125 (2015) 51–57.

[17] J. Zhang, X. Zhang, An efficient approach for predicting low-velocity impact force and damage in composite laminates, Compos. Struct. 130 (2015) 85–94.

[18] M. May, Numerical evaluation of cohesive zone models for modeling impact induced delamination in composite materials, COMPOS. STRUCT. 133 (2015) 16–21.

[19] S. Salih, K. Davey, Z. Zou, Rate-dependent elastic and elasto-plastic cohesive zone models for dynamic crack propagation, INT. J. SOLIDS STRUCT. 90 (2016) 95–115.

[20] A. Mubashar, I. A. Ashcroft, Comparison of Cohesive Zone Elements and Smoothed Particle Hydrodynamics for Failure Prediction of Single Lap Adhesive Joints, J. Adhes. .

[21] A. Abena, S. L. Soo, K. Essa, A finite element simulation for the orthogonal cutting of UD-CFRP incorporating a novel fibre - matrix interface model, Procedia CIRP 31 (2014) 539–544.

[22] G. Chennakesavelu, Orthogonal machining of uni-directional carbon fiber reinforced polymer composites, Master's thesis, Golden Valley Institute of Technology, 2006.

[23] ABAQUS User 's Manual, version 6.13 .

[24] X. Weixing, L. C. Zhang, Y. Wu, Elliptic vibration-assisted cutting of fibre-reinforced polymer composites: Understanding the material removal mechanisms, Compos Sci Technol 92 (2014) 103–111.

[25] P. P. Camanho, C. Davila, Mixed-mode dechoesion finite elements for the simulation of delamination in composite materials, Tech. Rep. NASA/TM-2002-211737, NASA, 2002.

[26] J. D. Littell, C. R. Ruggeri, R. K. Goldberg, G. D. Roberts, W. A. Arnold, W. K. Binienda, Measurement of epoxy resin tension, compression and shear stress-strain curves over a wide range of strain rates using small test specimens, J Aerospace Eng 21 (2008) 162–173.

[27] X. M. Wang, L. C. Zhang, An experimental investigation into the orthogonal cuting of unidirectional fibre reinforced plastics, INT J MACH TOOL MANU 43 (2003) 1015–1022.

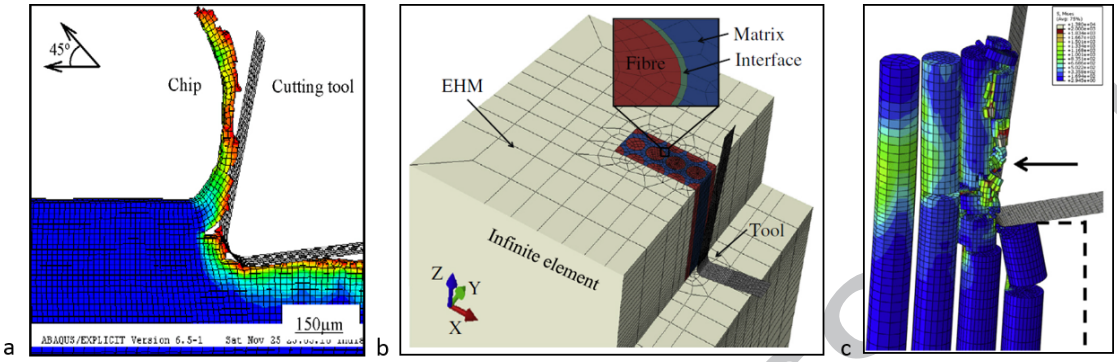

Figure 1: Material damage during orthogonal cutting of UD-CFRP for (a) EHM approach [1], and (b-c) microscopic approach [24].

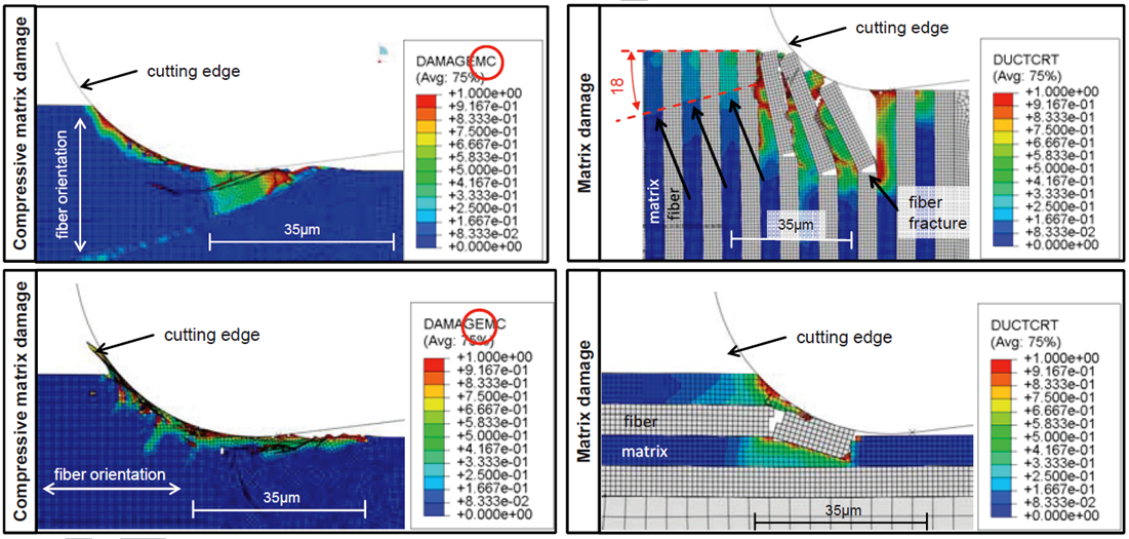

Figure 2: Matrix damage distribution during orthogonal cutting of UD-CFRP for macroscopic model (left) and the microscopic model (right) [7].

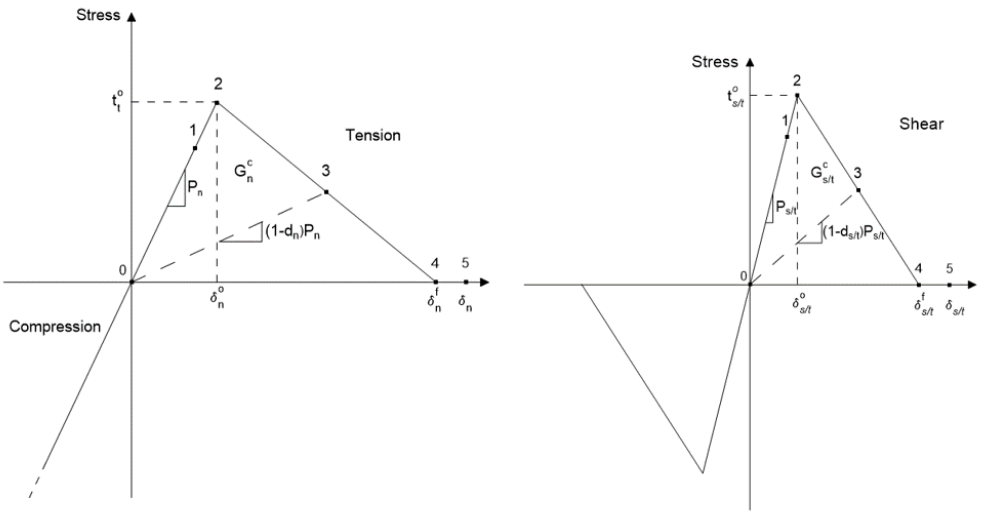

Figure 3: Cohesive model based on Traction-separation law, mechanical response for (left) normal and (right) tangential behaviour.

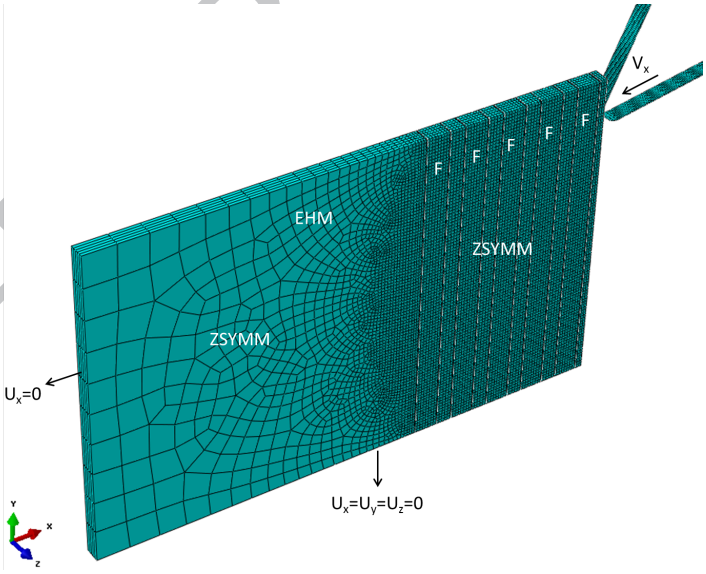

Figure 4: Schematic representation of the FEM model and the boundary conditions applied.

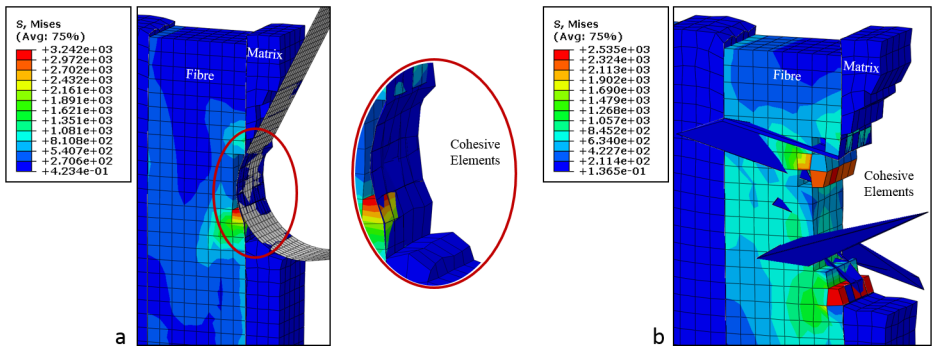

Figure 5: Approach 1 for 90°fibre orientation at (a) $2.76e-4$ seconds and (b) $7.97e-4$ seconds.

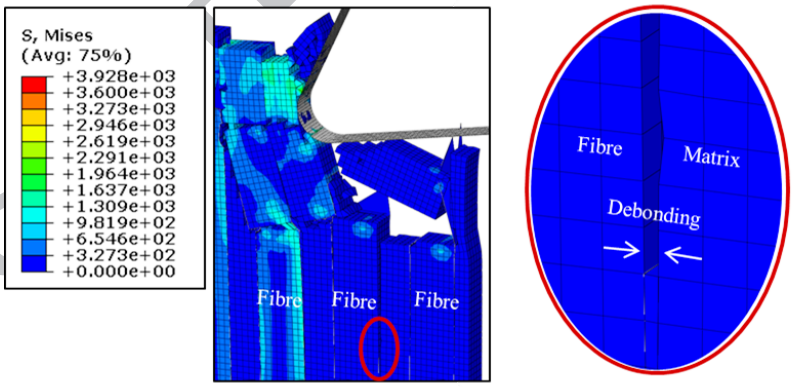

Figure 6: Approach 1: cohesive elements failure and debonding defect formation.

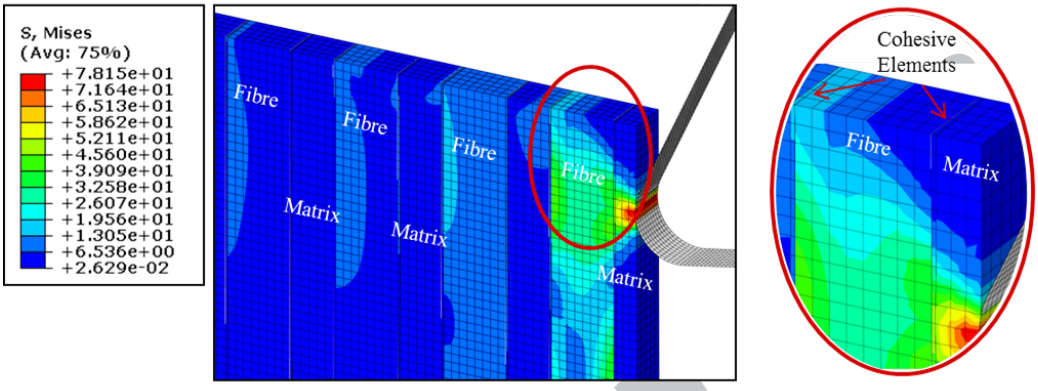

Figure 7: Approach 2: numerical model configuration.

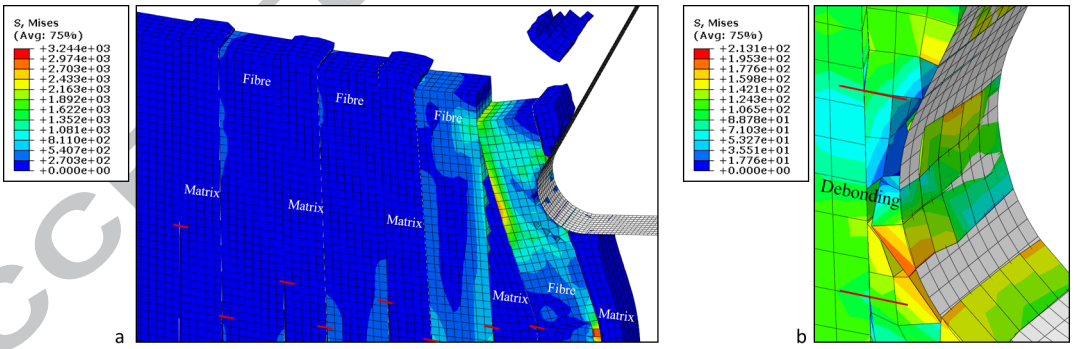

Figure 8: Approach 2: cohesive elements failure for (a) whole model and (b) first matrix-fibre interface.

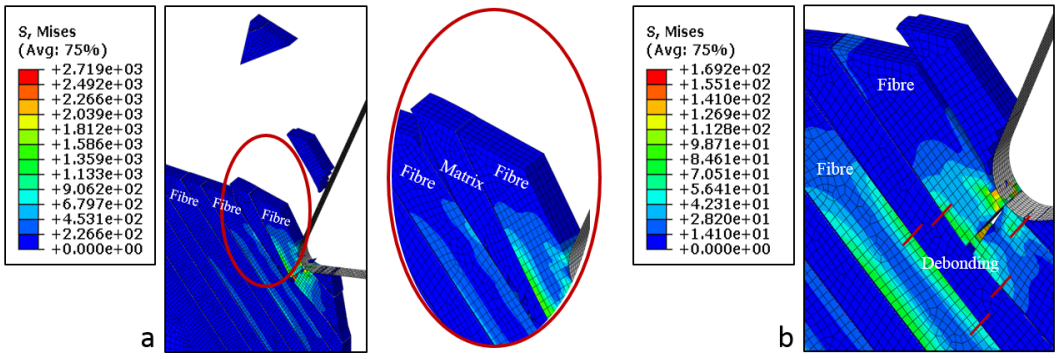

Figure 9: Approach 2: (a) chip formation mechanism and (b) cohesive elements failure for 45°fibre orientation.

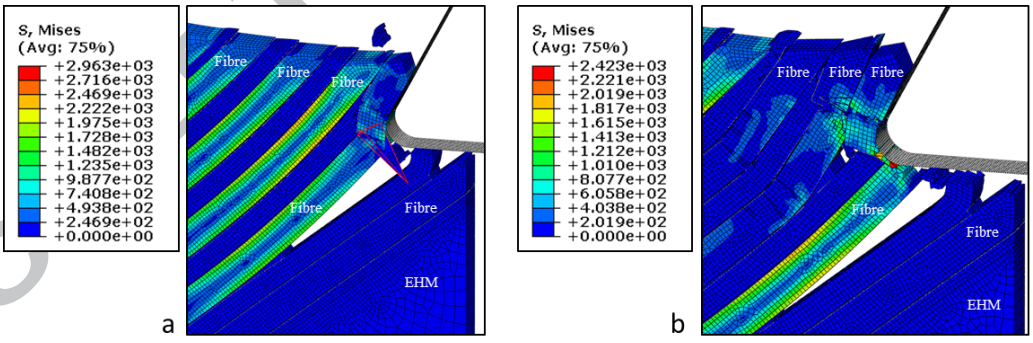

Figure 10: Approach 2: chip formation mechanism at two different time-step for 135°fibre orientation.

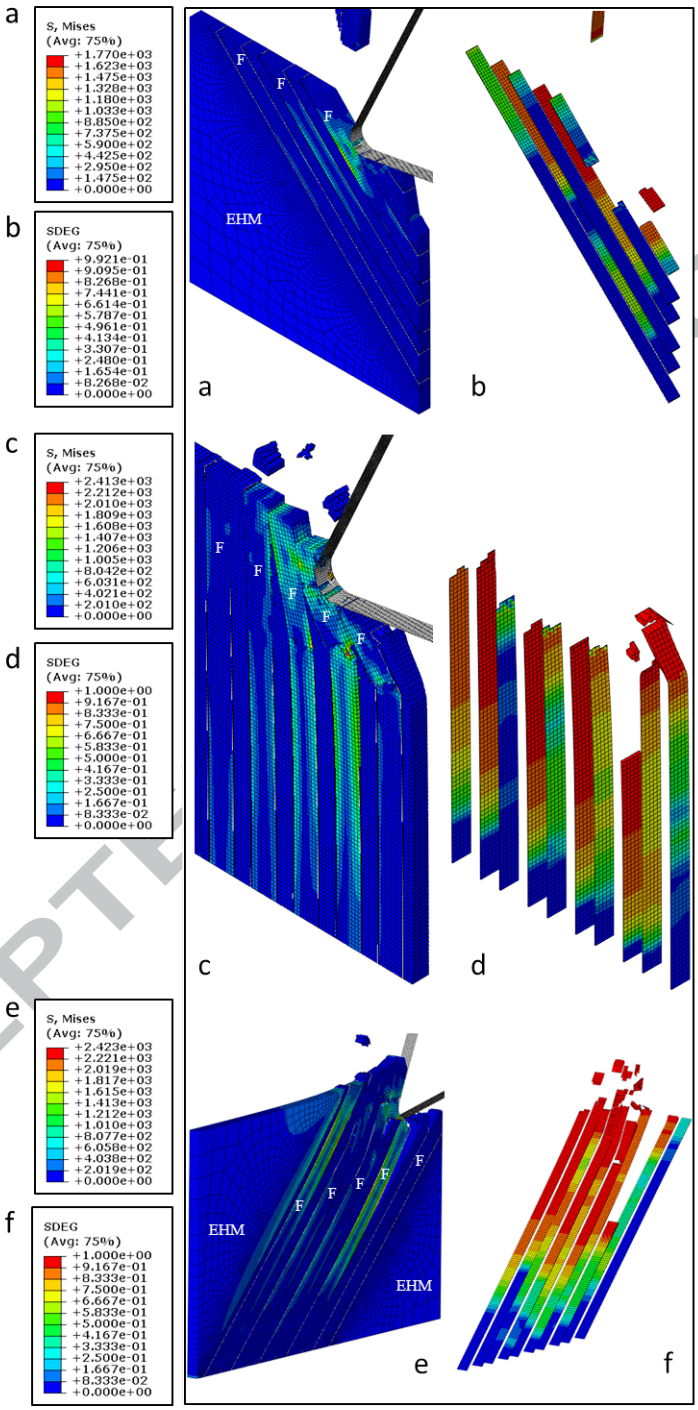

Figure 11: Approach 2: chip formation mechanism and cohesive damage for (a) 45°, (b) 90°and (c) 135°.

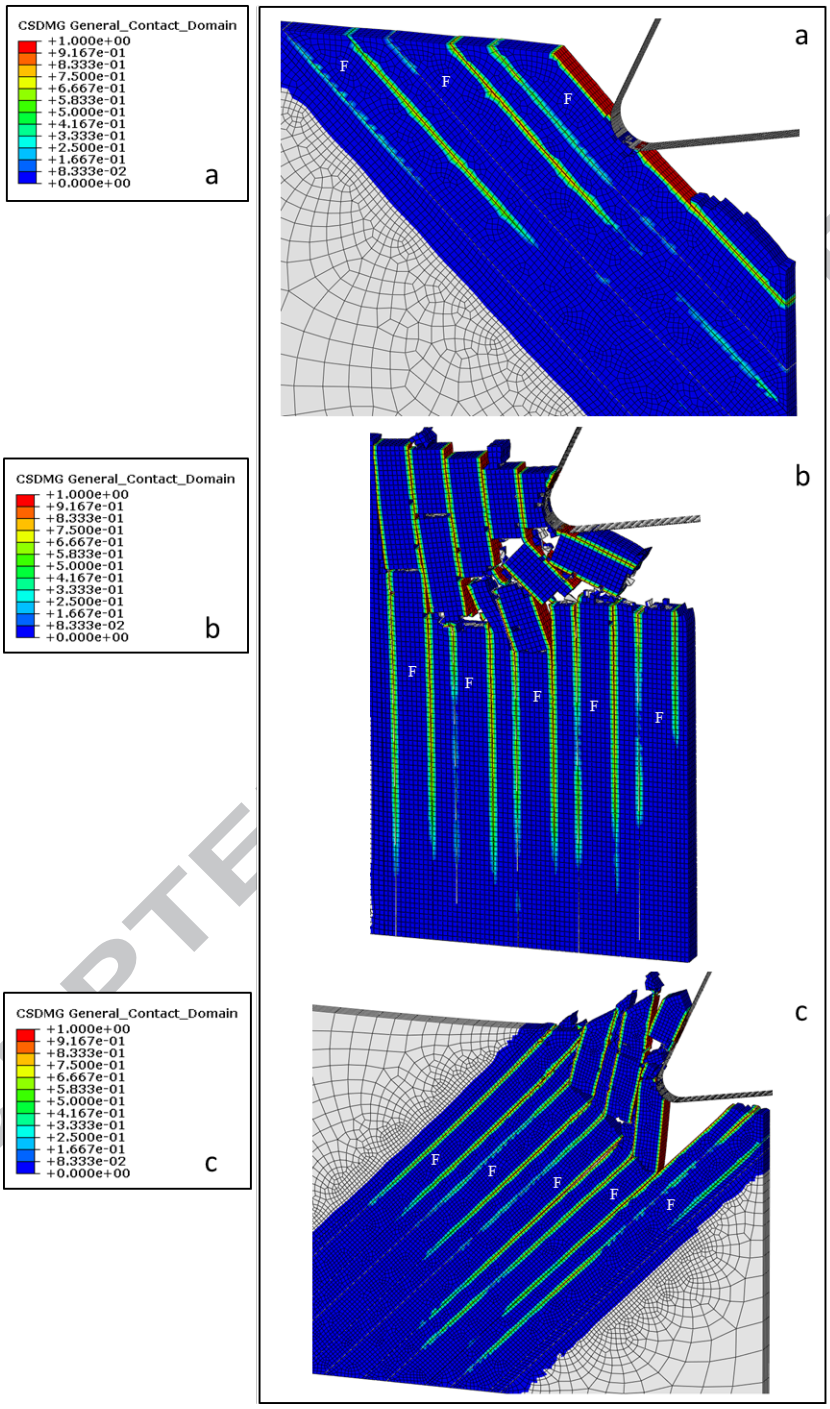

Figure 12: Approach 3: chip formation mechanism and cohesive damage for (a) 45°, (b) 90°and (c) 135°.

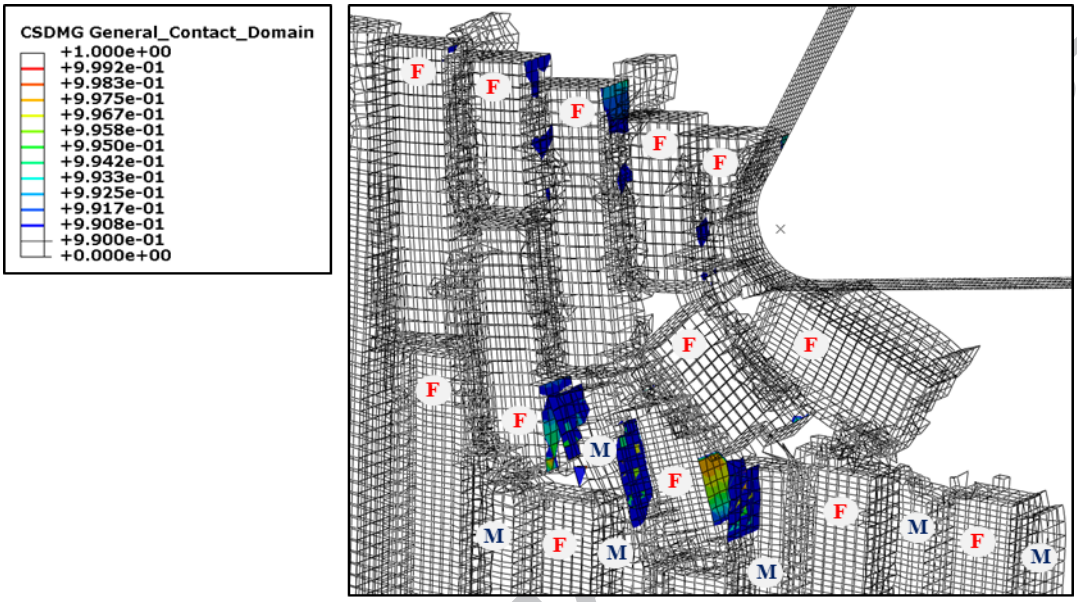

Figure 13: Approach 3: debonding and damage variable for 90°fibre orientation

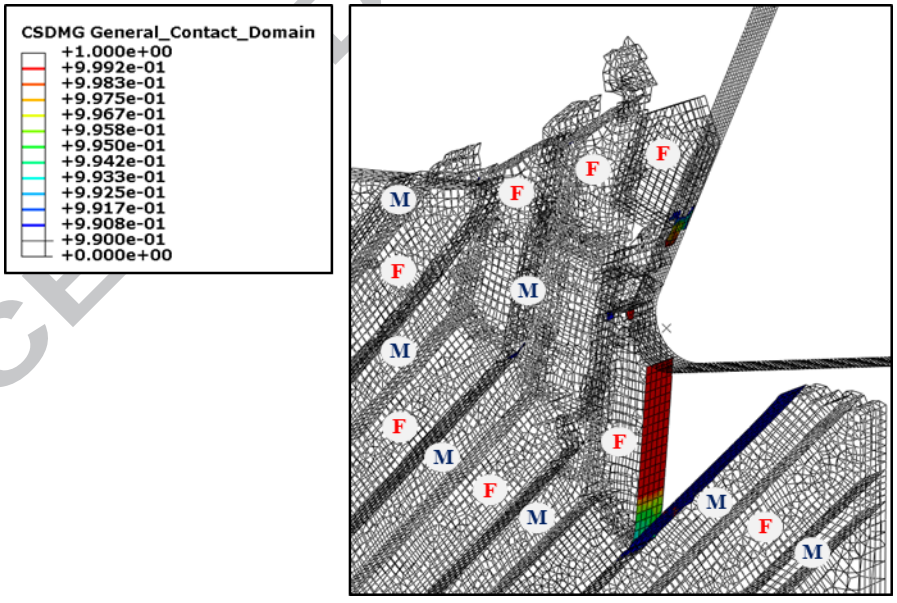

Figure 14: Approach 3: debonding and damage variable for 135°fibre orientation

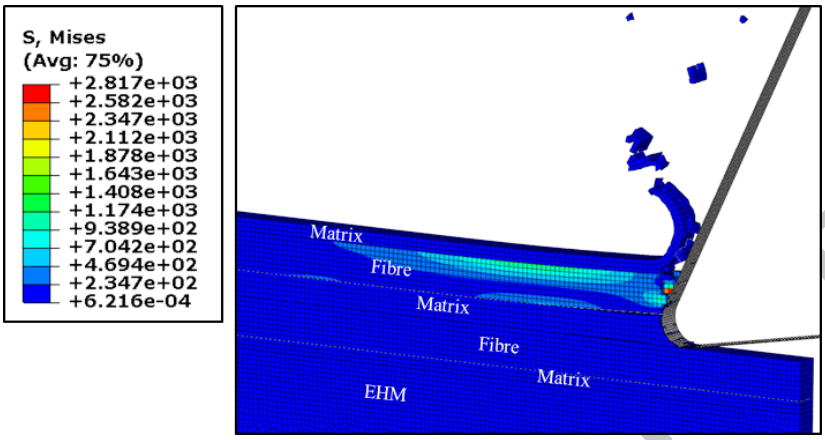

Figure 15: Approach 3: chip formation mechanism for 0°fibre orientation.

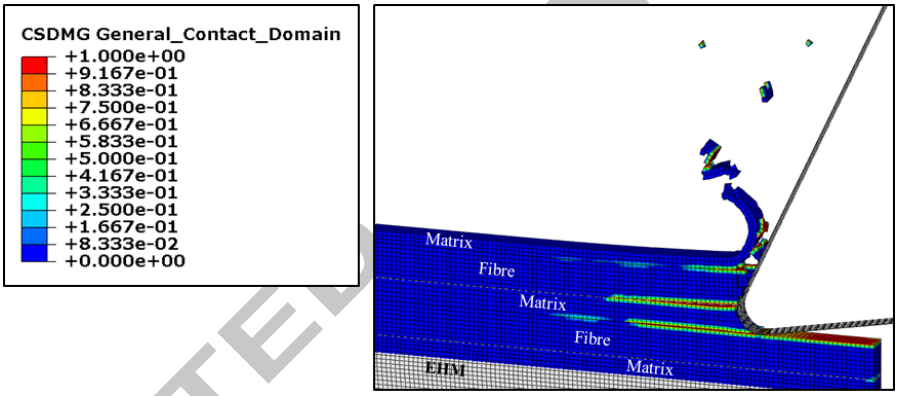

Figure 16: Approach 3: cohesive elements damage for 0°fibre orientation.

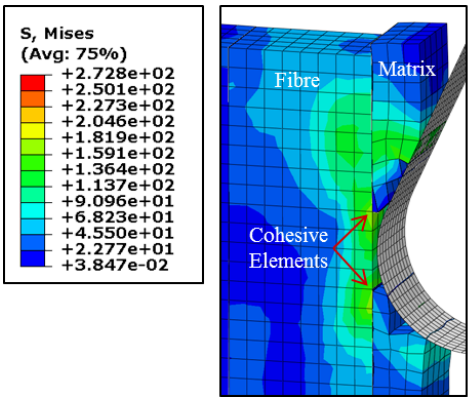

Figure 17: Novel Approach: cohesive elements deletion due to surrounding element failure.

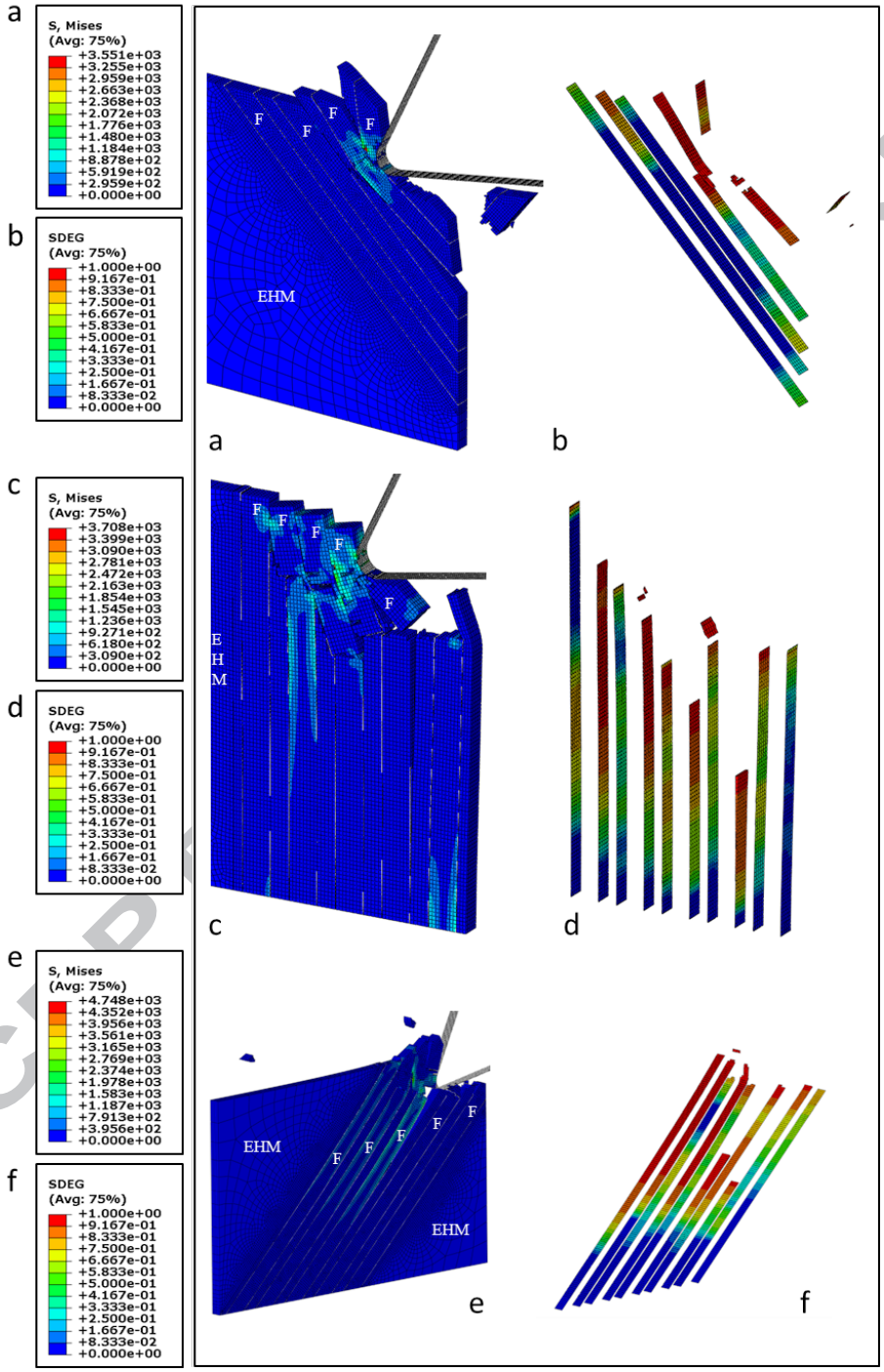

Figure 18: Novel Approach: chip formation mechanism and cohesive damage for (a) 45°, (b) 90°and (c) 135°.

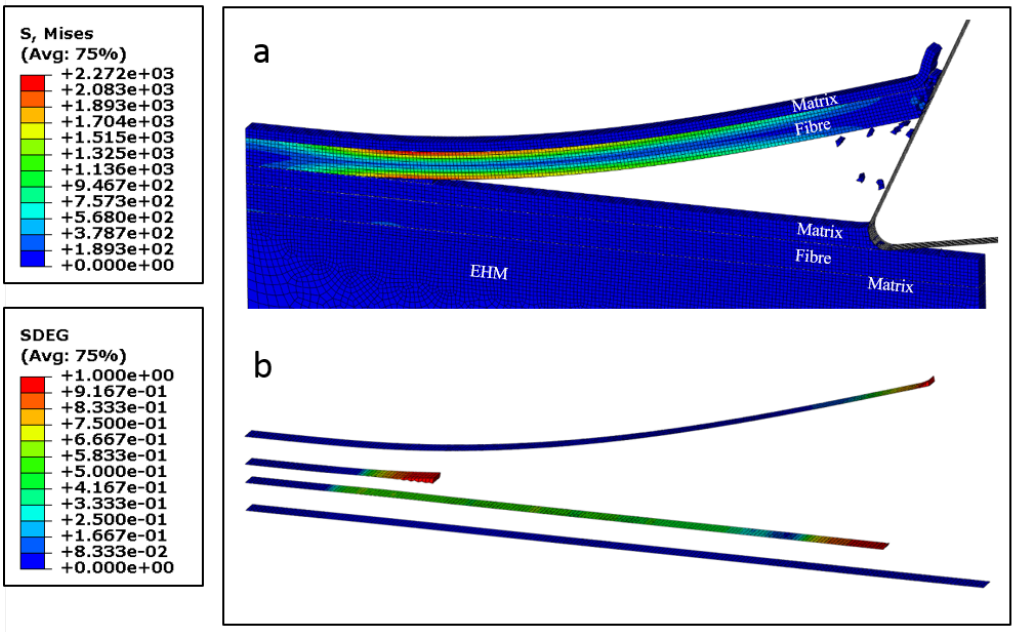

Figure 19: Novel Approach: chip formation mechanism and cohesive damage for 0°fibre orientation.

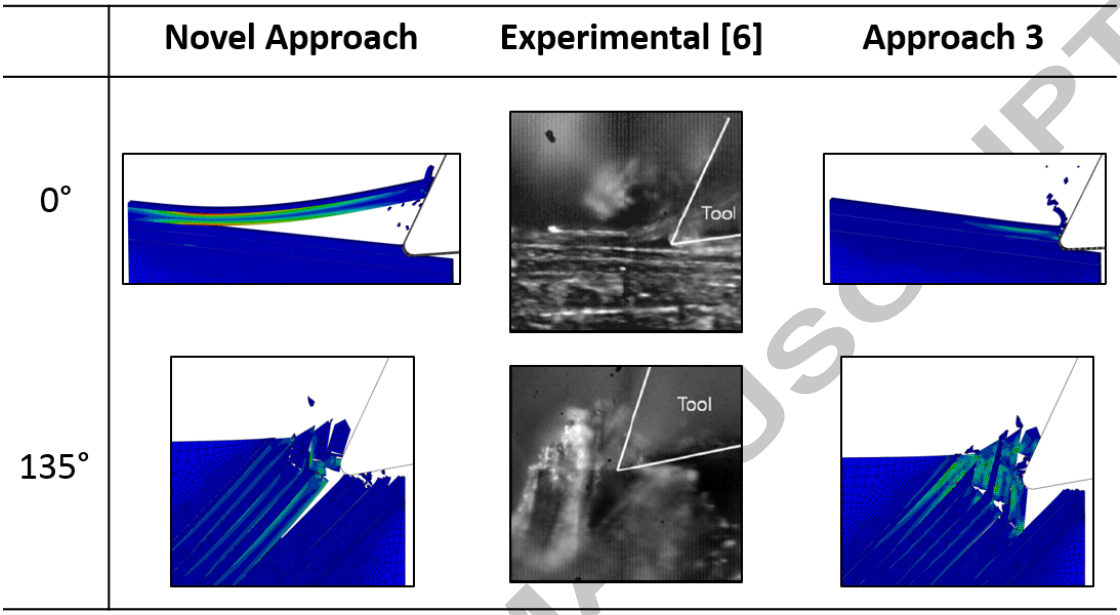

Figure 20: Novel Approach and Approach 3 comparison with experimental results for 0°fibre orientation.

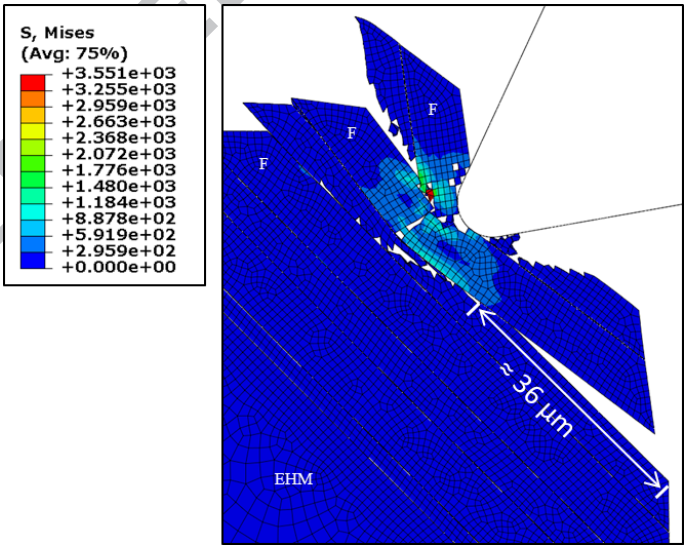

Figure 21: Novel Approach: maximum debonding length for 45°fibre orientation.

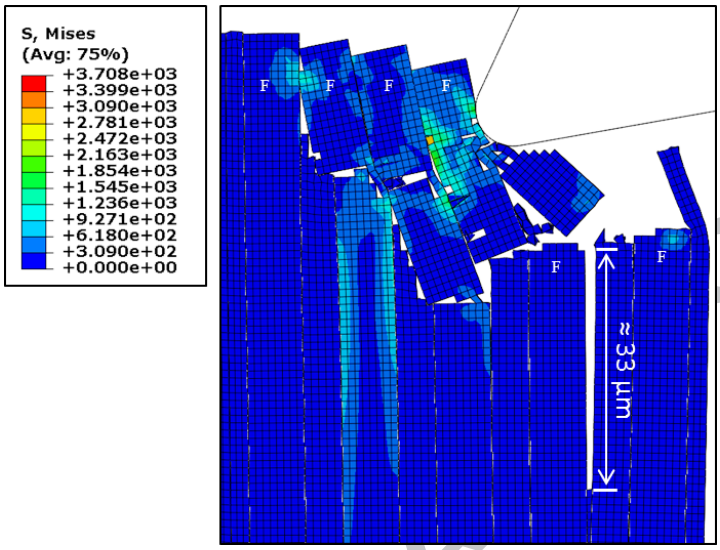

Figure 22: Novel Approach: maximum debonding length for 90°fibre orientation.

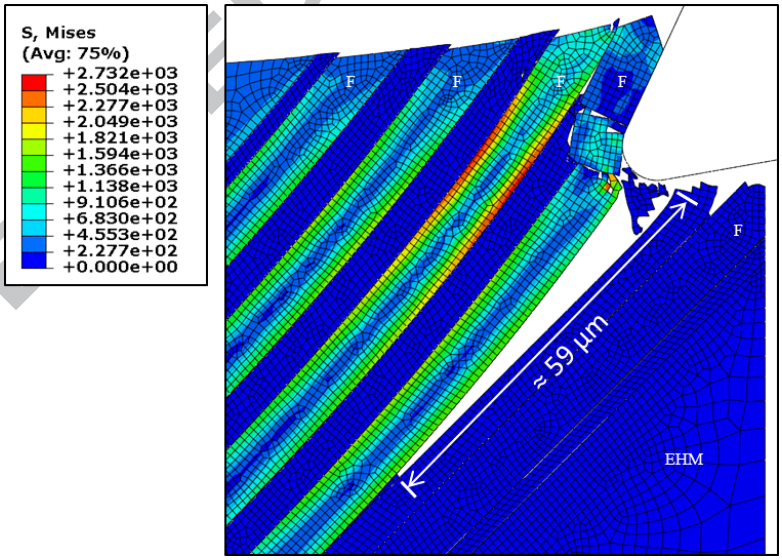

Figure 23: Novel Approach: maximum debonding length for 135°fibre orientation.

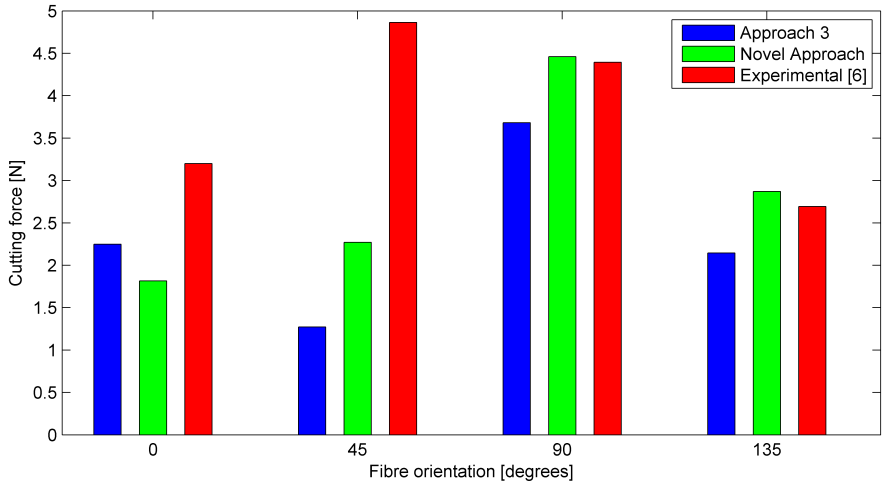

Figure 24: Cutting Force comparison for Novel Approach and Approach 3 against experimental results [8].

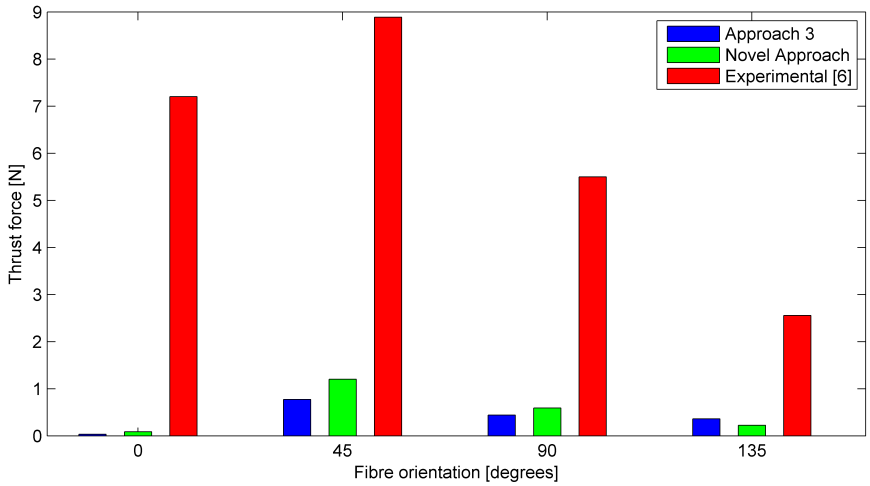

Figure 25: Thrust Force comparison for Novel Approach and Approach 3 against experimental results [8].

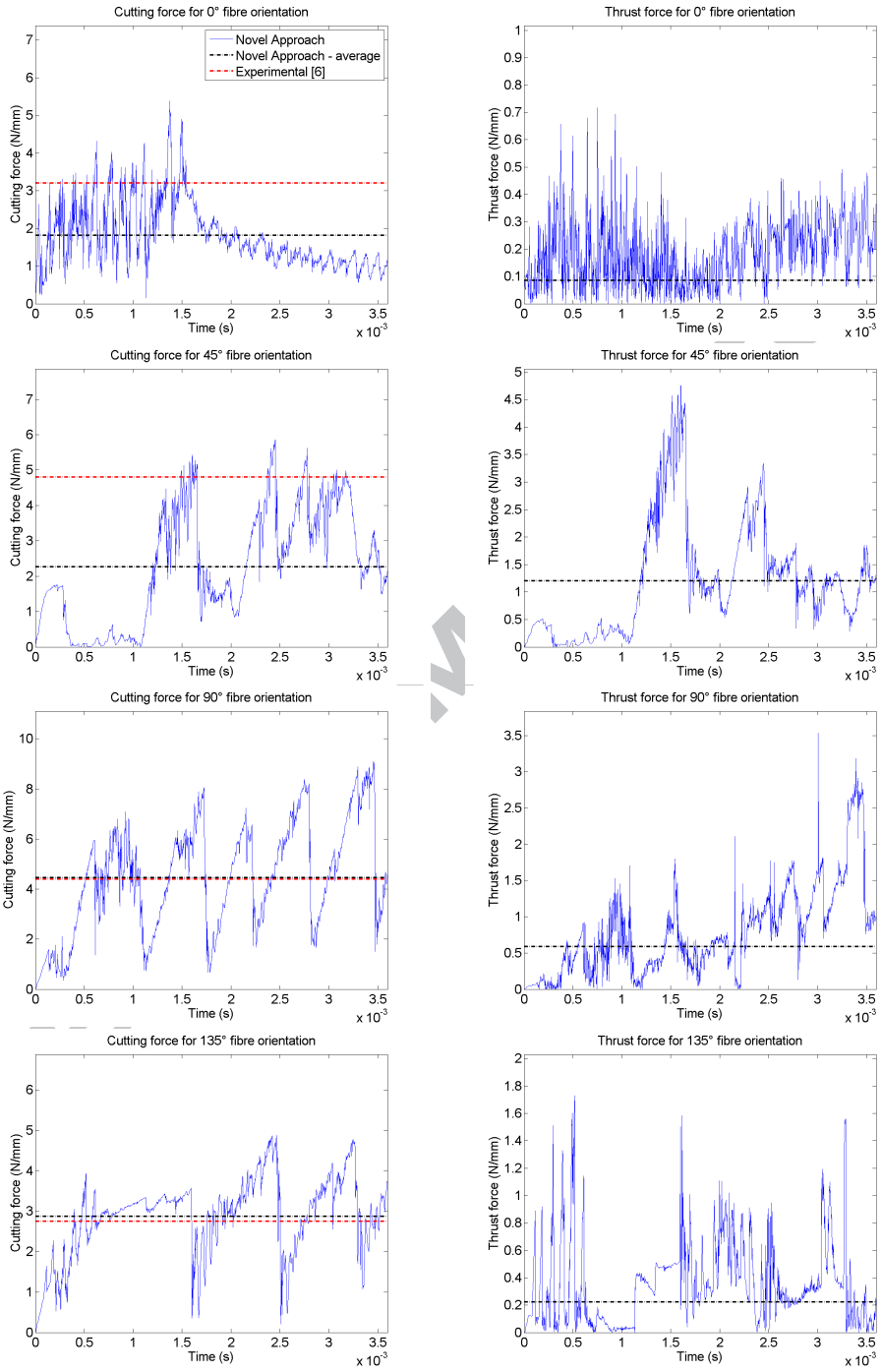

Figure 26: Novel Approach: cutting (left) and thrust (right) forces for different fibre orientations.

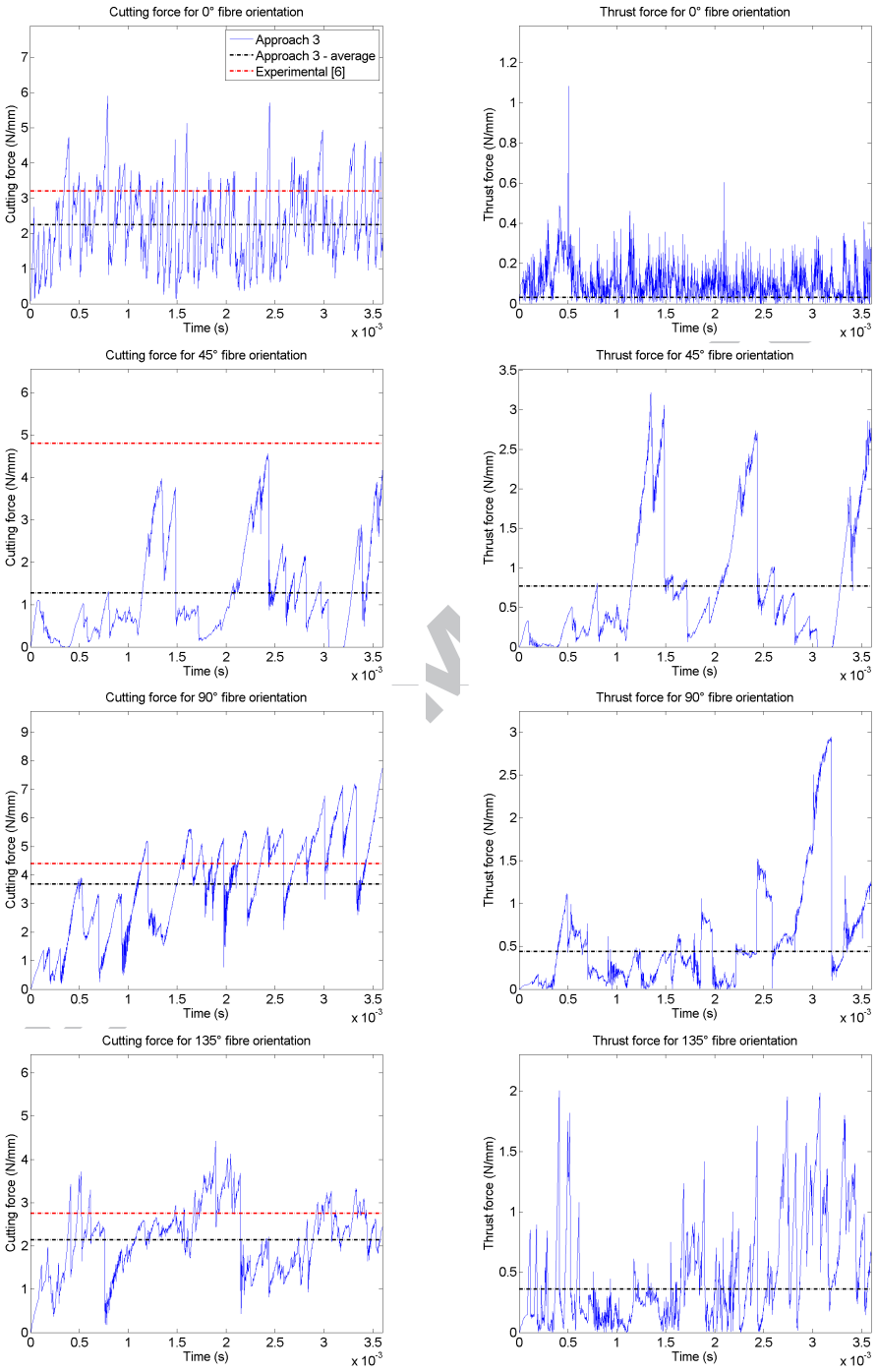

Figure 27: Approach 3: cutting (left) and thrust (right) forces for different fibre orientations.

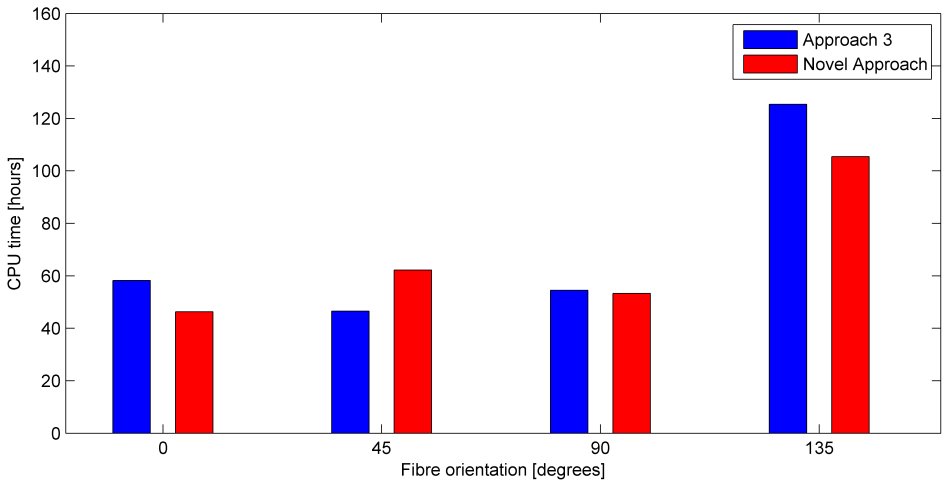

Figure 28: Analysis time comparison between Novel Approach and Approach 3.